CHALMERS

UNIVERSITY OF TECHNOLOGY

Huygens' surface excitation for the finite element method applied to Maxwell's equations – A construction based on Nitsche's method

N.B. When citing this work, cite the original published paper.

(article starts on next page)

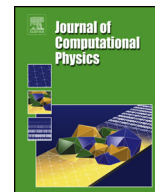# Huygens' surface excitation for the finite element method applied to Maxwell's equations – A construction based on Nitsche's method

Johan Winges, Thomas Rylander *

Department of Electrical Engineering, Chalmers University of Technology, SE-41296 Göteborg, Sweden

ARTICLE INFO

ABSTRACT

We present a Huygens' surface for the finite element method applied to Maxwell's equations, where the equivalent electric and magnetic surface currents are incorporated in the weak form by means of Nitsche's method. The proposed method preserves the reciprocity of Maxwell's equations and it allows for the computation of the total field inside the Huygens' surface, whereas on its outside only the scattered field is computed. The equivalent magnetic surface current at the Huygens' surface requires a double representation of the discontinuous tangential component of the electric field and we demonstrate that it can be efficiently combined with a previously presented higher-order brick-tetrahedron hybridization. Also, it is demonstrated that the near-to-far-field transformation can be evaluated in an accurate manner if collocated with the Huygens' surface, which allows for a compact computational domain and a reduction in the required computational resources. The proposed Huygens' surface is tested on two scattering problems with perfect electric conductor scatterers: (i) a sphere that demonstrates second-order convergence towards the analytical result for a piecewise linear approximation of the electric field; and (ii) a double ogive with two sharp tips which gives a computed monostatic radar cross section that compares well with measurements and computations in the open literature for both polarizations.

1. Introduction

Electromagnetic scattering has a history of more than 100 years, where the pioneering work by Mie [1] is very well-known and has had an enormous impact in many scientific disciplines. Today, the modern and increasingly powerful computational resources allow for the numerical solution of ever more difficult scattering problems, where the development of new numerical algorithms has made it possible to address entirely new challenges in terms of scatterers with complicated geometry and media. Kahnert [2] provides a rather recent review of numerical methods for electromagnetic scattering problems, where both differential and integral equation are considered.

The finite element method (FEM) [3] is well-suited for problems with complicated geometry and media, where non-linear media can be treated in the time domain. In the context of scattering (and radiation) problems in free space, the computational mesh must be truncated and efficient techniques are available [3], where the perfectly matched layer (PML) [4,5] is

---

* Corresponding author.
  E-mail address: rylander@chalmers.se (T. Rylander).

very popular since it preserves the sparsity of the system of linear equations and can be formulated in the time domain [6]. However, the PML is not suitable for the implementation of an incident field and, thus, it must be complemented by other techniques when applied to scattering problems.

The so-called scattered field formulation for the FEM is a rather direct approach as it solves for the scattered field in the entire computational domain, where the incident field enters the formulation as an inhomogeneous Dirichlet boundary condition on metal surfaces and as volume sources in dielectric media. However, this approach is not well-suited for very complicated surfaces or penetrable inhomogeneous media, where the sources are computationally expensive to evaluate. In the case of media with non-linearities, time-domain computations are necessary and it may be impossible to compute the time-dependent volumetric sources since the scattered field formulation relies on the linearity of the Maxwell's equations. For problems such as well-shielded cavities or efficiently shadowing structures, the scattered field almost cancels the incident field and, thus, the post-process construction of the total field may suffer from severe numerical inaccuracies.

An elegant solution to these problems is to use a so-called Huygens' surface, which encloses the scatterer and is entirely located in the free-space region that embeds the scatterer. This technique has been very popular to use for the finite-difference time-domain (FDTD) scheme [7,8], where efficient time-domain implementations are possible. The Huygens' surface is equipped with equivalent electric and magnetic surface currents that are computed from the incident field such that they yield the total field inside and the scattered field outside the Huygens' surface. This type of approach can also be used for the FEM, which has been described by Marchand et al. [9] and references therein. Marchand et al. use the finite-element tearing-and-interconnect (FETI) approach to implement the magnetic surface currents that are necessary to establish an electric field with a discontinuous tangential component on the Huygens' surface. Their approach also involves an extra unknown field on the Huygens' surface and this field can be interpreted as the Lagrangian multiplier featured in the conventional FETI [10] expressed as constrained variational principle. Marchand et al. [9] only test their method for two-dimensional problems with transverse electric (TE) fields, although they point out that the formulation may be generalized to three-dimensional cases too.

In this article, we present and test a new technique to implement a Huygens' surface for the FEM applied to Maxwell's equations in three dimensions. We use Nitsche's method [11,12] to impose equivalent electric and magnetic surface currents on the Huygens' surface. These equivalent surface currents are related to a tangential discontinuity in the magnetic and electric fields, respectively, according to the equivalence principle. As a consequence, we compute the total electric field inside the Huygens' surface and the scattered electric field outside the Huygens' surface. For the FEM, we use curl-conforming elements [13] for the total-field region and the scattered-field region separately, where we have two sets of degrees of freedom for the tangential electric field at the Huygens' surface to allow for the discontinuity associated with the equivalent magnetic surface current. This construction in combination with Galerkin's method preserves the reciprocity of the continuous system.

In particular, the Huygens' surface proposed in this article can be collocated with the hybrid interface between an unstructured mesh of tetrahedrons and a structured grid of brick-shaped elements, where this hybrid interface is featured by our previously presented higher-order hybrid method [14] that combines body-conforming tetrahedrons with brick-shaped elements [6] that allow for mass lumping. In addition, we demonstrate that it is possible to also apply the near-to-far-field transformation [8] at the surface that is also used for both the hybrid interface and the Huygens' surface, which reduces the size of the computational domain. In this computational setting, our proposed Huygens' surface is tested on the (bistatic) scattering from a perfect electric conducting sphere and the computed results are compared with the Mie solution [1,15]. In addition, we compute the monostatic radar cross section for the double ogive at 1.57 GHz and 9 GHz, which is one of the EMCC radar benchmark cases [16].

2. Method

As illustrated in Fig. 1, the computational domain Ω is partitioned into two sub-regions: (i) the total field region Ω^{tot}; and (ii) the scattered-field region Ω^{sca}. Here, the interface between Ω^{tot} and Ω^{sca} is denoted by Γ_{H}, which is referred to as a Huygens' surface. We formulate the problem in the frequency domain and the corresponding time-domain version of the method can be directly derived by means of the Fourier transform. In the total field region Ω^{tot}, we wish to compute the total electric field $\boldsymbol{E}^{\text{tot}} = \boldsymbol{E}^{\text{inc}} + \boldsymbol{E}^{\text{sca}}$, where $\boldsymbol{E}^{\text{inc}}$ is the incident field and $\boldsymbol{E}^{\text{sca}}$ is the scattered field. In contrast, we wish to compute only the scattered field $\boldsymbol{E}^{\text{sca}}$ in the scattered-field region Ω^{sca}.

Here, the sources that cause the incident field $\boldsymbol{E}^{\text{inc}}$ are assumed to be located at infinity and, thus, $\boldsymbol{E}^{\text{inc}}$ has no sources inside the computational domain Ω. Given only these sources, the incident field $\boldsymbol{E}^{\text{inc}}$ is the solution to Maxwell's equations in free space and, in particular, the incident field $\boldsymbol{E}^{\text{inc}}$ is then known throughout the computational domain Ω. For the (trivial) problem without scatterers, we then have $\boldsymbol{E}^{\text{tot}} = \boldsymbol{E}^{\text{inc}}$ in Ω^{tot} and $\boldsymbol{E}^{\text{sca}} = \boldsymbol{0}$ in Ω^{sca}. Next, the scatterers of interest are placed in the total field region Ω^{tot} and these scatterers cause a (non-zero) scattered field $\boldsymbol{E}^{\text{sca}}$, where the scattered field $\boldsymbol{E}^{\text{sca}}$ has its (fictitious) sources located inside Γ_{H}. It should be emphasized that outside Γ_{H}, the total electric field can easily be computed once the scattered field $\boldsymbol{E}^{\text{sca}}$ is known and, as a consequence, it is sufficient to compute the scattered field $\boldsymbol{E}^{\text{sca}}$ in Ω^{sca}. Finally, we wish to work with the total field $\boldsymbol{E}^{\text{tot}}$ in Ω^{tot} since it is typically easier to model complicated materials or impose boundary conditions in terms of the total field. For further information on scattering problems and their solution, the reader is recommended the excellent book by Kristensson [17]. The construction based on the total field and the scattered field presented above is very common to use for scattering problems formulated in terms of partial differential
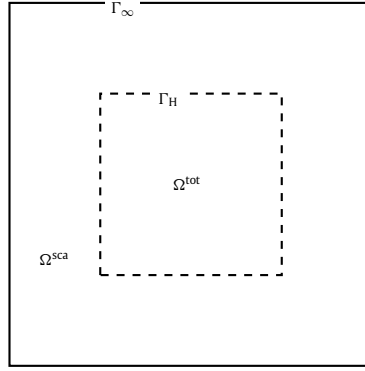
Fig. 1. Computational domain partitioned into a total-field region Ω^{tot} and a scattered-field region Ω^{sca}.

equations, where the reader is recommended the book by Taflove and Hagness [8] for formulations suitable for the FDTD scheme.

In addition, we use the notation

$$
\boldsymbol{E} = \begin{cases} \boldsymbol{E}^{\text{tot}} & \text{in } \Omega^{\text{tot}} \\ \boldsymbol{E}^{\text{sca}} & \text{in } \Omega^{\text{sca}} \end{cases}
\tag{1}
$$

for the field solution throughout the entire computational domain Ω, which features a discontinuity in the tangential component of the electric field at the Huygens' surface Γ_{H}.

The total electric field $\boldsymbol{E}^{\text{tot}}$ must satisfy the vector Helmholtz' equation in Ω^{tot}, which is derived from Maxwell's equations based on the constitutive relations and the fact that Faraday's law then can be used to eliminate the magnetic field in Ampère's law. Similarly, $\boldsymbol{E}^{\text{sca}}$ must satisfy the vector Helmholtz' equation in Ω^{sca}, which is a consequence of the fact that the incident field $\boldsymbol{E}^{\text{inc}}$ already satisfies the vector Helmholtz' equation with its sources outside Ω. In summary, we have two (disjoint) partial differential equations

$$
\nabla \times (\mu^{-1} \nabla \times \boldsymbol{E}^{\text{tot}}) - \omega^2 \epsilon \boldsymbol{E}^{\text{tot}} = \boldsymbol{0} \qquad \text{in } \Omega^{\text{tot}}
\tag{2}
$$

$$
\nabla \times (\mu_0^{-1} \nabla \times \boldsymbol{E}^{\text{sca}}) - \omega^2 \epsilon_0 \boldsymbol{E}^{\text{sca}} = \boldsymbol{0} \qquad \text{in } \Omega^{\text{sca}}
\tag{3}
$$

Next, the two field solutions $\boldsymbol{E}^{\text{tot}}$ and $\boldsymbol{E}^{\text{sca}}$ are related to each other by two interface conditions on Γ_{H}. Given Eq. (1), we introduce the notation $[\![\boldsymbol{E}]\!] = \boldsymbol{E}^{\text{sca}} - \boldsymbol{E}^{\text{tot}} = -\boldsymbol{E}^{\text{inc}}$ for the so-called jump of $\boldsymbol{E}$ at Γ_{H}. By definition, we then get the interface condition $\hat{\boldsymbol{n}} \times [\![\boldsymbol{E}]\!] = -\hat{\boldsymbol{n}} \times \boldsymbol{E}^{\text{inc}}$ on Γ_{H} for the electric field itself, where $\hat{\boldsymbol{n}} = \hat{\boldsymbol{n}}^{\text{sca}} = -\hat{\boldsymbol{n}}^{\text{tot}}$ is the unit normal vector associated with Γ_{H} and it points away from Ω^{sca}. Similarly, we get the interface condition $\hat{\boldsymbol{n}} \times [\![\nabla \times \boldsymbol{E}]\!] = -\hat{\boldsymbol{n}} \times \nabla \times \boldsymbol{E}^{\text{inc}}$ on Γ_{H} for the curl of the electric field. In summary, we have two interface conditions

$$
\hat{\boldsymbol{n}} \times [\![\boldsymbol{E}]\!] = \boldsymbol{P}_{\text{H}} \qquad \text{on } \Gamma_{\text{H}}
\tag{4}
$$

$$
\hat{\boldsymbol{n}} \times [\![\nabla \times \boldsymbol{E}]\!] = \boldsymbol{Q}_{\text{H}} \qquad \text{on } \Gamma_{\text{H}}
\tag{5}
$$

where $\boldsymbol{P}_{\text{H}} = -\hat{\boldsymbol{n}} \times \boldsymbol{E}^{\text{inc}}$ and $\boldsymbol{Q}_{\text{H}} = -\hat{\boldsymbol{n}} \times \nabla \times \boldsymbol{E}^{\text{inc}}$ are computed from the given incident field $\boldsymbol{E}^{\text{inc}}$. Alternatively, the equivalent magnetic surface current $\boldsymbol{M}_s = \boldsymbol{P}_{\text{H}}$ and the electric surface currents $\boldsymbol{J}_s = \boldsymbol{Q}_{\text{H}}/(j\omega\mu_0)$ could be used to represent the sources outside the Huygens' surface that cause the incident field.

The boundary value problem (2)-(5) without any scatterers obviously gives the solution $\boldsymbol{E}^{\text{inc}}$ in Ω^{tot} and the zero solution in Ω^{sca}, since the scattered field is zero for such a situation. An actual scattering problem of practical interest requires the boundary value problem (2)-(5) to be complemented with additional information that is intentionally omitted below in the derivation of the Huygens' surface (cf. Sec. 2.1), since it simplifies the presentation. Thus, we would need to, given an actual scattering problem, place the scatterer in the interior of Ω^{tot} and apply a free-space truncation of Ω^{sca} at its outer boundary Γ_{∞}. Thus, Eq. (2) may involve inhomogeneous material parameters μ and ϵ in the interior of Ω^{tot}, should Ω^{tot} contain penetrable scatterers. In addition, the interior of Ω^{tot} may feature additional boundary conditions that model, e.g., perfect electric conductor (PEC) surfaces or waveguide ports associated with antennas. The outer boundary Γ_{∞} of the computational domain is equipped with some sort of free-space truncation and, for the numerical tests in this article, we use a PML backed by a PEC. For other options on free-space truncation of the finite element mesh for electromagnetic problems, the reader is referred to the book by Jin [3].

2.1. Finite element formulation using Nitsche's method

Here, we derive the weak form for the boundary value problem (2)-(5). First, we define the function spaces [13,18]

$$\boldsymbol{H}(\mathrm{curl}, \Omega^{\mathrm{tot}}) = \left\{ \boldsymbol{E}^{\mathrm{tot}} : \int_{\Omega^{\mathrm{tot}}} |\boldsymbol{E}^{\mathrm{tot}}|^2 d\Omega^{\mathrm{tot}} < \infty \text{ and } \int_{\Omega^{\mathrm{tot}}} |\nabla \times \boldsymbol{E}^{\mathrm{tot}}|^2 d\Omega^{\mathrm{tot}} < \infty \right\} \text{ and} \tag{6}$$

$$\boldsymbol{H}_0(\mathrm{curl}, \Omega^{\mathrm{sca}}) = \left\{ \boldsymbol{E}^{\mathrm{sca}} : \int_{\Omega^{\mathrm{sca}}} |\boldsymbol{E}^{\mathrm{sca}}|^2 d\Omega^{\mathrm{sca}} < \infty \text{ and } \int_{\Omega^{\mathrm{sca}}} |\nabla \times \boldsymbol{E}^{\mathrm{sca}}|^2 d\Omega^{\mathrm{sca}} < \infty \text{ and } \hat{\boldsymbol{n}} \times \boldsymbol{E}^{\mathrm{sca}} = \boldsymbol{0} \text{ on } \Gamma_\infty \right\}. \tag{7}$$

We multiply Eq. (2) with the weighting function $\boldsymbol{W}_i^{\mathrm{tot}} \in \boldsymbol{H}(\mathrm{curl}, \Omega^{\mathrm{tot}})$ and integrate over Ω^{tot}. Next, we integrate by parts based on the identity $\nabla \cdot (\boldsymbol{u} \times \boldsymbol{v}) = (\nabla \times \boldsymbol{u}) \cdot \boldsymbol{v} - \boldsymbol{u} \cdot (\nabla \times \boldsymbol{v})$ and Gauss' theorem. This yields

$$\int_{\Omega^{\mathrm{tot}}} \left(\nabla \times \boldsymbol{W}_i^{\mathrm{tot}}\right) \cdot \left(\mu^{-1} \nabla \times \boldsymbol{E}^{\mathrm{tot}}\right) - \omega^2 \boldsymbol{W}_i^{\mathrm{tot}} \cdot \left(\epsilon \boldsymbol{E}^{\mathrm{tot}}\right) d\Omega^{\mathrm{tot}} + \int_{\Gamma_{\mathrm{H}}} \left(\hat{\boldsymbol{n}} \times \boldsymbol{W}_i^{\mathrm{tot}}\right) \cdot \left(\mu_0^{-1} \nabla \times \boldsymbol{E}^{\mathrm{tot}}\right) d\Gamma_{\mathrm{H}} = 0, \tag{8}$$

where we assume that $\mu = \mu_0$ in the immediate (infinitesimal) neighborhood of Γ_{H} as it is approached from Ω^{tot}. Similarly, we multiply Eq. (3) with the weighting function $\boldsymbol{W}_i^{\mathrm{sca}} \in \boldsymbol{H}_0(\mathrm{curl}, \Omega^{\mathrm{sca}})$ and integrate over Ω^{sca}. Next, we integrate by parts again in combination with the boundary condition $\hat{\boldsymbol{n}} \times \boldsymbol{E}^{\mathrm{sca}} = \boldsymbol{0}$ on Γ_∞, which yields

$$\int_{\Omega^{\mathrm{sca}}} \left(\nabla \times \boldsymbol{W}_i^{\mathrm{sca}}\right) \cdot \left(\mu_0^{-1} \nabla \times \boldsymbol{E}^{\mathrm{sca}}\right) - \omega^2 \boldsymbol{W}_i^{\mathrm{sca}} \cdot \left(\epsilon_0 \boldsymbol{E}^{\mathrm{sca}}\right) d\Omega^{\mathrm{sca}} - \int_{\Gamma_{\mathrm{H}}} \left(\hat{\boldsymbol{n}} \times \boldsymbol{W}_i^{\mathrm{sca}}\right) \cdot \left(\mu_0^{-1} \nabla \times \boldsymbol{E}^{\mathrm{sca}}\right) d\Gamma_{\mathrm{H}} = 0. \tag{9}$$

In summary, we have the two separate expressions

$$\left(\nabla \times \boldsymbol{W}_i^{\mathrm{tot}}, \mu^{-1} \nabla \times \boldsymbol{E}^{\mathrm{tot}}\right)_{\Omega^{\mathrm{tot}}} - \omega^2 \left(\boldsymbol{W}_i^{\mathrm{tot}}, \epsilon \boldsymbol{E}^{\mathrm{tot}}\right)_{\Omega^{\mathrm{tot}}} + \left(\hat{\boldsymbol{n}} \times \boldsymbol{W}_i^{\mathrm{tot}}, \mu_0^{-1} \nabla \times \boldsymbol{E}^{\mathrm{tot}}\right)_{\Gamma_{\mathrm{H}}} = 0 \text{ and} \tag{10}$$

$$\left(\nabla \times \boldsymbol{W}_i^{\mathrm{sca}}, \mu_0^{-1} \nabla \times \boldsymbol{E}^{\mathrm{sca}}\right)_{\Omega^{\mathrm{sca}}} - \omega^2 \left(\boldsymbol{W}_i^{\mathrm{sca}}, \epsilon_0 \boldsymbol{E}^{\mathrm{sca}}\right)_{\Omega^{\mathrm{sca}}} - \left(\hat{\boldsymbol{n}} \times \boldsymbol{W}_i^{\mathrm{sca}}, \mu_0^{-1} \nabla \times \boldsymbol{E}^{\mathrm{sca}}\right)_{\Gamma_{\mathrm{H}}} = 0, \tag{11}$$

which apply to the two separate sub-domains Ω^{tot} and Ω^{sca}, respectively, without regard to the interface conditions (4)-(5) at the Huygens' surface Γ_{H}. It should be emphasized that the permeability is assumed to be μ_0 at the interface Γ_{H} and in its immediate (infinitesimal) neighborhood inside Ω^{tot}. Here and in the following, $(\boldsymbol{u}, \boldsymbol{v})_X = \int_X \boldsymbol{u} \cdot \boldsymbol{v} \, dX$ denotes the inner product of $\boldsymbol{u}$ and $\boldsymbol{v}$ on the region X, where X may be a sub-domain or an interface between two sub-domains.

We add Eqs. (10)-(11) to arrive at the weak form

$$\left(\nabla \times \boldsymbol{W}_i^{\mathrm{tot}}, \mu^{-1} \nabla \times \boldsymbol{E}^{\mathrm{tot}}\right)_{\Omega^{\mathrm{tot}}} + \left(\nabla \times \boldsymbol{W}_i^{\mathrm{sca}}, \mu_0^{-1} \nabla \times \boldsymbol{E}^{\mathrm{sca}}\right)_{\Omega^{\mathrm{sca}}} - \omega^2 \left(\boldsymbol{W}_i^{\mathrm{tot}}, \epsilon \boldsymbol{E}^{\mathrm{tot}}\right)_{\Omega^{\mathrm{tot}}} - \omega^2 \left(\boldsymbol{W}_i^{\mathrm{sca}}, \epsilon_0 \boldsymbol{E}^{\mathrm{sca}}\right)_{\Omega^{\mathrm{sca}}}$$

$$+ \left(\hat{\boldsymbol{n}} \times \boldsymbol{W}_i^{\mathrm{tot}}, \mu_0^{-1} \nabla \times \boldsymbol{E}^{\mathrm{tot}}\right)_{\Gamma_{\mathrm{H}}} - \left(\hat{\boldsymbol{n}} \times \boldsymbol{W}_i^{\mathrm{sca}}, \mu_0^{-1} \nabla \times \boldsymbol{E}^{\mathrm{sca}}\right)_{\Gamma_{\mathrm{H}}} = 0 \tag{12}$$

To incorporate the interface conditions (4)-(5) at Γ_{H}, we use the two average operators $\{\!\{\boldsymbol{E}\}\!\} = \kappa_1 \boldsymbol{E}^{\mathrm{sca}} + \kappa_2 \boldsymbol{E}^{\mathrm{tot}}$ and $\{\!\{\boldsymbol{E}\}\!\}^\circledast = \kappa_2 \boldsymbol{E}^{\mathrm{sca}} + \kappa_1 \boldsymbol{E}^{\mathrm{tot}}$, cf. Wadbro et al. [19]. Here, the non-negative values κ_1 and κ_2 can be chosen given the constraint that $\kappa_1 + \kappa_2 = 1$. Given these definitions, we have that

$$\boldsymbol{u}^{\mathrm{sca}} \cdot \boldsymbol{v}^{\mathrm{sca}} - \boldsymbol{u}^{\mathrm{tot}} \cdot \boldsymbol{v}^{\mathrm{tot}} = \{\!\{\boldsymbol{u}\}\!\} \cdot [\![\boldsymbol{v}]\!] + [\![\boldsymbol{u}]\!] \cdot \{\!\{\boldsymbol{v}\}\!\}^\circledast = \{\!\{\boldsymbol{u}\}\!\}^\circledast \cdot [\![\boldsymbol{v}]\!] + [\![\boldsymbol{u}]\!] \cdot \{\!\{\boldsymbol{v}\}\!\}$$

for any two fields $\boldsymbol{u}$ and $\boldsymbol{v}$ on the interface Γ_{H}, where the notation presented in Eq. (1) is applied to both $\boldsymbol{u}$ and $\boldsymbol{v}$. Thus, we may express the surface terms associated with Γ_{H} in Eq. (12) by

$$\left(\hat{\boldsymbol{n}} \times \boldsymbol{W}_i^{\mathrm{tot}}, \mu_0^{-1} \nabla \times \boldsymbol{E}^{\mathrm{tot}}\right)_{\Gamma_{\mathrm{H}}} - \left(\hat{\boldsymbol{n}} \times \boldsymbol{W}_i^{\mathrm{sca}}, \mu_0^{-1} \nabla \times \boldsymbol{E}^{\mathrm{sca}}\right)_{\Gamma_{\mathrm{H}}}$$

$$= -\left(\hat{\boldsymbol{n}} \times \{\!\{\boldsymbol{W}_i\}\!\}^\circledast, \mu_0^{-1} [\![\nabla \times \boldsymbol{E}]\!]\right)_{\Gamma_{\mathrm{H}}} - \left(\hat{\boldsymbol{n}} \times [\![\boldsymbol{W}_i]\!], \mu_0^{-1} \{\!\{\nabla \times \boldsymbol{E}\}\!\}\right)_{\Gamma_{\mathrm{H}}}$$

$$= \left(\{\!\{\boldsymbol{W}_i\}\!\}^\circledast, \mu_0^{-1} \boldsymbol{Q}_{\mathrm{H}}\right)_{\Gamma_{\mathrm{H}}} - \left(\hat{\boldsymbol{n}} \times [\![\boldsymbol{W}_i]\!], \mu_0^{-1} \{\!\{\nabla \times \boldsymbol{E}\}\!\}\right)_{\Gamma_{\mathrm{H}}}, \tag{13}$$

where we incorporate the interface condition (5). The second term in the right-hand side of Eq. (13) contributes to the system matrix and it is not symmetric. To render the final stiffness matrix symmetric and preserve the reciprocity in the discrete formulation of the problem, we exploit the interface condition (4) and subtract

$$\left(\{\!\{\nabla \times \boldsymbol{W}_i\}\!\}, \mu_0^{-1}(\hat{\boldsymbol{n}} \times [\![\boldsymbol{E}]\!] - \boldsymbol{P}_{\mathrm{H}})\right)_{\Gamma_{\mathrm{H}}} = 0 \tag{14}$$

from the weak form (12). In addition, the problem must be stabilized and this is accomplished by also adding

$$\gamma\left(\hat{\boldsymbol{n}}\times[\![\boldsymbol{W}_i]\!], \mu_0^{-1}h^{-1}(\hat{\boldsymbol{n}}\times[\![\boldsymbol{E}]\!] - \boldsymbol{P}_{\mathrm{H}})\right)_{\Gamma_{\mathrm{H}}} = 0, \tag{15}$$

to the weak form (12), which again is based on the fulfillment of the interface condition (4). Here, h is the element size and γ is a stabilization parameter that renders a stable problem for sufficiently large γ. The steps accounted for by Eqs. (14)-(15) are known as Nitsche's method [11,12].

We now solve the problem: seek $\boldsymbol{E}^{\mathrm{tot}} \in \boldsymbol{H}(\mathrm{curl}, \Omega^{\mathrm{tot}})$ and $\boldsymbol{E}^{\mathrm{sca}} \in \boldsymbol{H}_0(\mathrm{curl}, \Omega^{\mathrm{sca}})$ such that

$$
\begin{aligned}
&\left(\nabla\times\boldsymbol{W}_i^{\mathrm{tot}}, \mu^{-1}\nabla\times\boldsymbol{E}^{\mathrm{tot}}\right)_{\Omega^{\mathrm{tot}}} + \left(\nabla\times\boldsymbol{W}_i^{\mathrm{sca}}, \mu_0^{-1}\nabla\times\boldsymbol{E}^{\mathrm{sca}}\right)_{\Omega^{\mathrm{sca}}} - \omega^2\left(\boldsymbol{W}_i^{\mathrm{tot}}, \epsilon\boldsymbol{E}^{\mathrm{tot}}\right)_{\Omega^{\mathrm{tot}}} - \omega^2\left(\boldsymbol{W}_i^{\mathrm{sca}}, \epsilon_0\boldsymbol{E}^{\mathrm{sca}}\right)_{\Omega^{\mathrm{sca}}}\\
&\quad - \left(\hat{\boldsymbol{n}}\times[\![\boldsymbol{W}_i]\!], \mu_0^{-1}\{\!\{\nabla\times\boldsymbol{E}\}\!\}\right)_{\Gamma_{\mathrm{H}}} - \left(\{\!\{\nabla\times\boldsymbol{W}_i\}\!\}, \mu_0^{-1}\hat{\boldsymbol{n}}\times[\![\boldsymbol{E}]\!]\right)_{\Gamma_{\mathrm{H}}} + \gamma\left(\hat{\boldsymbol{n}}\times[\![\boldsymbol{W}_i]\!], \mu_0^{-1}h^{-1}\hat{\boldsymbol{n}}\times[\![\boldsymbol{E}]\!]\right)_{\Gamma_{\mathrm{H}}}\\
&= -\left(\{\!\{\boldsymbol{W}_i\}\!\}^{\circledast}, \mu_0^{-1}\boldsymbol{Q}_{\mathrm{H}}\right)_{\Gamma_{\mathrm{H}}} - \left(\{\!\{\nabla\times\boldsymbol{W}_i\}\!\}, \mu_0^{-1}\boldsymbol{P}_{\mathrm{H}}\right)_{\Gamma_{\mathrm{H}}} + \gamma\left(\hat{\boldsymbol{n}}\times[\![\boldsymbol{W}_i]\!], \mu_0^{-1}h^{-1}\boldsymbol{P}_{\mathrm{H}}\right)_{\Gamma_{\mathrm{H}}}
\end{aligned}
\tag{16}
$$

for all $\boldsymbol{W}_i^{\mathrm{tot}} \in \boldsymbol{H}(\mathrm{curl}, \Omega^{\mathrm{tot}})$ and $\boldsymbol{W}_i^{\mathrm{sca}} \in \boldsymbol{H}_0(\mathrm{curl}, \Omega^{\mathrm{sca}})$.

In order to arrive at a discrete problem, we expand the electric field according to $\boldsymbol{E}^{\mathrm{tot}} = \sum_j E_j^{\mathrm{tot}}\boldsymbol{N}_j^{\mathrm{tot}}$ on Ω^{tot} and $\boldsymbol{E}^{\mathrm{sca}} = \sum_j E_j^{\mathrm{sca}}\boldsymbol{N}_j^{\mathrm{sca}}$ on Ω^{sca}, where $\boldsymbol{N}_j^{\mathrm{tot}} \in \boldsymbol{H}(\mathrm{curl}, \Omega^{\mathrm{tot}})$ and $\boldsymbol{N}_j^{\mathrm{sca}} \in \boldsymbol{H}_0(\mathrm{curl}, \Omega^{\mathrm{sca}})$ are curl-conforming basis functions to be detailed later. Here, we wish to compute the unknown electric field coefficients E_j^{tot} and E_j^{sca}. We choose the weighting functions $\boldsymbol{W}_i^{\mathrm{tot}}$ from the set of basis functions $\boldsymbol{N}_j^{\mathrm{tot}}$ and, similarly, the weighting functions $\boldsymbol{W}_i^{\mathrm{sca}}$ from the set of basis functions $\boldsymbol{N}_j^{\mathrm{sca}}$, which corresponds to Galerkin's method. (It should be understood by now that the indexing of degrees of freedom, basis functions and weighting functions is different for Ω^{tot} and Ω^{sca}, despite that the same notation for the index is used in both sub-domains.)

Thus, the final weak formulation can be expressed as a system of linear equations

$$\left(\mathbf{S} - \mathbf{S}_{\mathrm{H},0} + \gamma\mathbf{S}_{\mathrm{H},\gamma} - \omega^2\mathbf{M}\right)\mathbf{e} = -\boldsymbol{q}_{\mathrm{H}} - \boldsymbol{p}_{\mathrm{H},0} + \gamma\,\boldsymbol{p}_{\mathrm{H},\gamma} \tag{17}$$

where $\mathbf{e}$ is a vector with the electric field coefficients E_j^{tot} and E_j^{sca} that we wish to compute. The matrix entries and remaining vector entries are given by

$$S_{ij} = \left(\nabla\times\boldsymbol{N}_i^{\mathrm{tot}}, \mu^{-1}\nabla\times\boldsymbol{N}_j^{\mathrm{tot}}\right)_{\Omega^{\mathrm{tot}}} + \left(\nabla\times\boldsymbol{N}_i^{\mathrm{sca}}, \mu_0^{-1}\nabla\times\boldsymbol{N}_j^{\mathrm{sca}}\right)_{\Omega^{\mathrm{sca}}}$$

$$S_{\mathrm{H},0,ij} = \left(\hat{\boldsymbol{n}}\times[\![\boldsymbol{N}_i]\!], \mu_0^{-1}\{\!\{\nabla\times\boldsymbol{N}_j\}\!\}\right)_{\Gamma_{\mathrm{H}}} + \left(\mu_0^{-1}\{\!\{\nabla\times\boldsymbol{N}_i\}\!\}, \hat{\boldsymbol{n}}\times[\![\boldsymbol{N}_j]\!]\right)_{\Gamma_{\mathrm{H}}},$$

$$S_{\mathrm{H},\gamma,ij} = \left(\hat{\boldsymbol{n}}\times[\![\boldsymbol{N}_i]\!], \mu_0^{-1}h^{-1}\hat{\boldsymbol{n}}\times[\![\boldsymbol{N}_j]\!]\right)_{\Gamma_{\mathrm{H}}},$$

$$M_{ij} = \left(\boldsymbol{N}_i^{\mathrm{tot}}, \epsilon\boldsymbol{N}_j^{\mathrm{tot}}\right)_{\Omega^{\mathrm{tot}}} + \left(\boldsymbol{N}_i^{\mathrm{sca}}, \epsilon_0\boldsymbol{N}_j^{\mathrm{sca}}\right)_{\Omega^{\mathrm{sca}}}$$

$$q_{\mathrm{H},i} = \left(\{\!\{\boldsymbol{N}_i\}\!\}^{\circledast}, \mu_0^{-1}\boldsymbol{Q}_{\mathrm{H}}\right)_{\Gamma_{\mathrm{H}}},$$

$$p_{\mathrm{H},0,i} = \left(\{\!\{\nabla\times\boldsymbol{N}_i\}\!\}, \mu_0^{-1}\boldsymbol{P}_{\mathrm{H}}\right)_{\Gamma_{\mathrm{H}}},$$

$$p_{\mathrm{H},\gamma,i} = \left(\hat{\boldsymbol{n}}\times[\![\boldsymbol{N}_i]\!], \mu_0^{-1}h^{-1}\boldsymbol{P}_{\mathrm{H}}\right)_{\Gamma_{\mathrm{H}}}.$$

It should be noted that all matrices above are symmetric and, thus, the reciprocity of the continuum problem is preserved, which is a consequence of our formulation in combination with Galerkin's method.

2.2. Relation to the higher-order brick-tetrahedron hybrid

In Ref. [14], we present a higher-order brick-tetrahedron hybrid for Maxwell's equations. The Huygens' surface presented in this article reduces to this higher-order hybrid if $\boldsymbol{P}_{\mathrm{H}} = \boldsymbol{Q}_{\mathrm{H}} = \boldsymbol{0}$ and the total field region is discretized by tetrahedrons ($\Omega^{\mathrm{tot}} = \Omega^{\mathrm{tet}}$) whereas the scattered-field region is discretized by brick-shaped elements ($\Omega^{\mathrm{sca}} = \Omega^{\mathrm{hex}}$), which implies that the hybrid interface Γ_{I} coincides with the Huygens' surface ($\Gamma_{\mathrm{I}} = \Gamma_{\mathrm{H}}$). In the following, we use this discretization since it provides three computational advantages:

1. Scatterers (and other physical objects) often involve complicated geometry and materials and, thus, it is advantageous to treat this part of the problem in terms of the total electric field expressed on an unstructured and body-conforming mesh of tetrahedrons, which also allows for local mesh-refinement where the solution may vary rapidly due to e.g. field singularities. It should be noted that our formulation allows for non-conforming meshes and function spaces at both Γ_{H} and Γ_{I}, which can be useful in cases that require local mesh-refinement in the vicinity of the Huygens' surface and/or the hybrid interface.
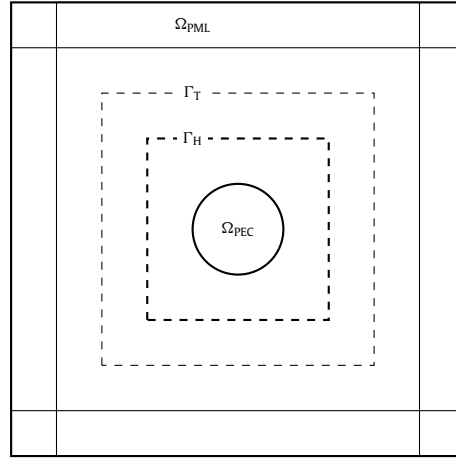
Fig. 2. Computational domain for the scattering problem: (i) thick solid circle – PEC scatterer that occupies the sub-domain Ω_{PEC}; (ii) thick dashed line – Huygens' surface Γ_H that is collocated with the hybrid interface Γ_I in all tests in this article; (iii) thin dashed line – near-to-far-field transformation surface Γ_T; (iv) thick solid square box – computational domain truncated at Γ_∞ by a PEC equipped with a PML region Ω_{PML} for the absorption of the outward propagating scattered field.

2. The computational region that surrounds the scatterers (and other objects) consists typically of free-space and, thus, it is desirable to use brick-shaped elements that allow for efficient computations in large homogeneous regions. In addition, it is favorable to compute the scattered field in this region since it allows for direct usage of a wide variety of methods to truncate the computational domain for free-space problems.

3. The formulation of the Huygens' surface requires two sets of degrees of freedom to represent the discontinuity of the tangential electric field for the entire interface Γ_H. Also, the hybrid interface Γ_I that connects the structured grid of brick-shaped elements to the unstructured mesh of tetrahedrons requires a double representation of the tangential field on the interface [14], which is a consequence of the different curl-conforming spaces that describe the tangential electric field on the triangular and the rectangular faces that coincide with the hybrid interface. The collocation of the Huygens' surface Γ_H with the hybrid interface Γ_I requires only *one* double representation for the tangential field. Also, this type of arrangement often brings the Huygens' surface rather close to the scatterers, which in turn reduces the size of the interface with the double representation. Finally, the accumulation of dispersion errors is also mitigated by a shorter distance between the Huygens' surface and the scatterer.

It should be noted that problems with several disjoint scatterers may be treated by a separate Huygens' surface with a hybrid interface for each individual scatterer, where the homogeneous regions between the scatterers can be treated by a grid of structured brick-shaped elements.

3. Results

We test the Huygens' surface formulation on two scattering problems with PEC scatterers: (i) a sphere; and (ii) a double ogive. The scattering problem with the PEC sphere can be solved analytically on closed form [1,15], which allows for an assessment of the error in the numerical solution. The double ogive features two sharp tips that support field singularities and it has a very low monostatic radar cross section, which makes it a useful and interesting test case since it provides additional challenges for the numerical solution of the scattering problem. Before the numerical results are presented, we describe the test-case setup with reference to the computational domain for the scattering problem shown in Fig. 2, where the PEC scatterer occupies the domain Ω_{PEC}.

The total field region Ω^{tot} is located inside the Huygens' surface Γ_H, which is shown by a thick dashed line in Fig. 2. Here, we typically discretize a relatively thin layer next to the scatterer's surface by tetrahedrons and, in this article, we employ the hierarchical basis functions presented by Ingelström [20]. This unstructured mesh is body conforming to the surface of the scatterer and we use an isoparametric representation of curved surfaces as higher-order basis functions are used to represent the electric field. In the following, we denote the polynomial order of the basis functions by p^{tet} for the tetrahedrons. The lowest-order curl-conforming elements are, thus, denoted by $p^{tet} = 1_i$, where the subindex i refers to that the basis is incomplete. Should the space of gradients be added to this set of basis functions, we have a complete linear representation of the electric field and the polynomial order is denoted by $p^{tet} = 1_c$, where the subindex c denotes that the basis is complete. Similarly, the quadratic basis is denoted $p^{tet} = 2_i$ if incomplete and $p^{tet} = 2_c$ if complete, etc.

Outside the Huygens' surface Γ_H, we solve for the scattered field in the homogeneous free-space region Ω^{sca}. Here, Ω^{sca} is discretized with brick-shaped elements of incomplete order $p^{hex} = 1_i, 2_i, \ldots$. This construction allows for mass lumping [6] that renders the mass matrix diagonal, which reduces the memory requirements and allows for explicit time-

stepping. Given that we solve for the scattered field in Ω^{sca}, there is a number of possibilities for the free-space truncation of the computational grid. Here, we use a PML [21,22] terminated by a PEC at Γ_∞ and we employ the PML formulation for Cartesian coordinates with the diagonal material tensors $\bar{\bar{\epsilon}} = \epsilon_0 \bar{\bar{\Lambda}}$ and $\bar{\bar{\mu}} = \mu_0 \bar{\bar{\Lambda}}$ [21,22], where

$$\bar{\bar{\Lambda}} = \hat{\boldsymbol{x}} \left(\frac{\gamma_y \gamma_z}{\gamma_x} \right) \hat{\boldsymbol{x}} + \hat{\boldsymbol{y}} \left(\frac{\gamma_x \gamma_z}{\gamma_y} \right) \hat{\boldsymbol{y}} + \hat{\boldsymbol{z}} \left(\frac{\gamma_x \gamma_y}{\gamma_z} \right) \hat{\boldsymbol{z}}. \tag{18}$$

Given the orthogonal distance ζ_a from the PML-vacuum interface into the PML, we have $\gamma_a(\zeta_a) = 1 + \sigma_a(\zeta_a)/(j\omega\epsilon_0)$ for the Cartesian axes a = x, y and z. Further, we use a quadratic profile for the PML conductivity $\sigma_a(\zeta_a) = \sigma_{a,\max}(\zeta_a/L_a)^2$, where L_a is the thickness of the PML layer. In the following, we specify the desired reflection coefficient R_0 at normal incidence and, given an idealized theoretical analysis [23] of the PML in the continuum case, we have $\sigma_{a,\max} = -(3\ln(R_0))/(2\eta_0 L_a)$, where $\eta_0 = \sqrt{\mu_0/\epsilon_0}$ is the impedance of vacuum.

The scatterer is illuminated by an incident plane wave $\boldsymbol{E}^{\text{inc}} = \hat{\boldsymbol{p}}^{\text{inc}} E_0 \exp(-jk_0 \hat{\boldsymbol{k}}^{\text{inc}} \cdot \boldsymbol{r})$ where the polarization is dictated by the unit vector $\hat{\boldsymbol{p}}^{\text{inc}}$ and the direction of propagation by $\hat{\boldsymbol{k}}^{\text{inc}}$. Here, the free-space wavenumber is denoted $k_0 = \omega/c_0$ and $\hat{\boldsymbol{p}}^{\text{inc}} \cdot \hat{\boldsymbol{k}}^{\text{inc}} = 0$. For this situation, we compute the bistatic radar cross section as a function of the elevation angle θ and azimuth angle ϕ in spherical coordinates, where the radar cross section is

$$\sigma(\theta, \phi) = \lim_{r \to \infty} 4\pi r^2 \frac{|\boldsymbol{E}^{\text{sca}}|^2}{|\boldsymbol{E}^{\text{inc}}|^2} = \frac{4\pi}{|E_0|^2}(|F_\theta(\theta, \phi)|^2 + |F_\phi(\theta, \phi)|^2).$$

Here, the radial coordinate in spherical coordinates is denoted by r and the scattered electric field in the far-field region is related to the far-field amplitude $\boldsymbol{F}$ by $\boldsymbol{E}^{\text{sca}} = r^{-1} \exp(-jk_0 r) \boldsymbol{F}$. The two components F_θ and F_ϕ (in spherical coordinates) of the far-field amplitude $\boldsymbol{F}$ are computed based on the scattered electromagnetic fields in the vicinity of the scatterer according to

$$\boldsymbol{F} = \frac{jk_0}{4\pi} \hat{\boldsymbol{r}} \times \oint_{\Gamma_{\text{T}}} \left[-\hat{\boldsymbol{n}} \times \boldsymbol{E}^{\text{sca}}(\boldsymbol{r}') + \eta_0 \hat{\boldsymbol{r}} \times (\hat{\boldsymbol{n}} \times \boldsymbol{H}^{\text{sca}}(\boldsymbol{r}')) \right] \exp(jk_0 \hat{\boldsymbol{r}} \cdot \boldsymbol{r}') \, d\Gamma',$$

where Γ_{T} is a closed surface that encloses the scatterer and $\hat{\boldsymbol{n}}$ is the unit normal to Γ_{T} that points away from the enclosed volume. Here, $\hat{\boldsymbol{r}} = \hat{\boldsymbol{r}}(\theta, \phi)$ is the unit radial vector that points in the direction for evaluation of $\sigma(\theta, \phi)$.

We use a curl-conforming basis to solve for the electric field $\boldsymbol{E}^{\text{sca}}$ in Ω^{sca} and, as a post-processing step, we compute the magnetic field by $\boldsymbol{H}^{\text{sca}} = -(j\omega\mu_0)^{-1}\nabla \times \boldsymbol{E}^{\text{sca}}$, where $\nabla \times \boldsymbol{E}^{\text{sca}}$ is discontinuous at the faces of the mesh. It is convenient to let the discretization and its faces conform to Γ_{T}, where the tangential component of the scattered electric field $\boldsymbol{E}^{\text{sca}}$ is easily accessed. For the magnetic field, we use $\boldsymbol{H}^{\text{sca}} = -(j\omega\mu_0)^{-1}\{\{\nabla \times \boldsymbol{E}^{\text{sca}}\}\}$ as it is evaluated on Γ_{T} with $\kappa_1 = \kappa_2 = 1/2$. It should be noted that it is feasible to let Γ_{T} coincide with Γ_{H} and, in that case, we must use $\boldsymbol{E}^{\text{sca}} = \boldsymbol{E}^{\text{tot}} - \boldsymbol{E}^{\text{inc}}$ in the region Ω^{tot} as the average $\{\{\nabla \times \boldsymbol{E}^{\text{sca}}\}\}$ is evaluated. Thus, this operation amounts to a simple post-processing step of subtracting the (known) incident field $\boldsymbol{E}^{\text{inc}}$ from the computed solution $\boldsymbol{E}^{\text{tot}}$, which is trivial and inexpensive from a computational point of view. One benefit of the choice $\Gamma_{\text{T}} = \Gamma_{\text{H}}$ is that it is feasible to shrink the computational domain and, thus, reduce the total number of degrees of freedom, which also lowers the computational cost.

In the following, we compute the electromagnetic fields by means of the weak formulation described in Sec. 2.1, where we use $\kappa_1 = 1$ with $\kappa_2 = 0$ since this choice typically results in fewer non-zero elements in the system matrix. Furthermore, the stabilization parameter γ is set to 10^3, which works well (with some margin) for all the numerical tests that follow where we use at most complete quadratic polynomial basis functions to approximate the electric field.

3.1. Sphere

First, we test the Huygens' surface for the scattering problem with a PEC sphere of radius $a = 1$ m. We perform a convergence test with respect to the cell size for the bistatic radar cross section computed at the frequency $f = 71.6$ MHz, which corresponds to $k_0 a = 1.5$. Here, we collocate Γ_{H} with the hybrid interface Γ_{I} and place $\Gamma_{\text{H}} = \Gamma_{\text{I}}$ rather close to the PEC sphere, which implies that it has a staircased shape as shown in Fig. 3 by the thick solid lines in the vicinity of the sphere. To facilitate comparisons with the literature [24], we choose Γ_{T} as the faces of a cube with the side length 3.2 m, where the PEC sphere is placed at the center of this region. Thus, Γ_{T} is completely located in the scattered-field region Ω^{sca}.

The computational domain is truncated at Γ_∞, which is constructed from the faces of a cube with the side length of 4.2 m that is also placed with the sphere at its center. On the outer boundary Γ_∞, we use a PEC boundary condition and the scattered field is absorbed by a PML of thickness $L_a = 0.1$ m with $N_{\text{PML}} = 4$ cells, which is placed inside and in direct contact with Γ_∞. For the PML, we set $\sigma_{a,\max}$ such that the reflection coefficient is $R_0 = 10^{-4}$ for normal incidence in the continuum case.

For the convergence test, we use cube-shaped elements of side length $h_n = h_1/n$ for $n = 1, 2, 3$ and 4, where $h_1 = 0.4$ m. The rest of the mesh is hierarchically refined in a similar fashion except for the PML region where we use $N_{\text{PML}} = 4$ cells in the direction perpendicular to Γ_∞ for all values of h_n. (Tests demonstrate that this type of discretized PML yields a
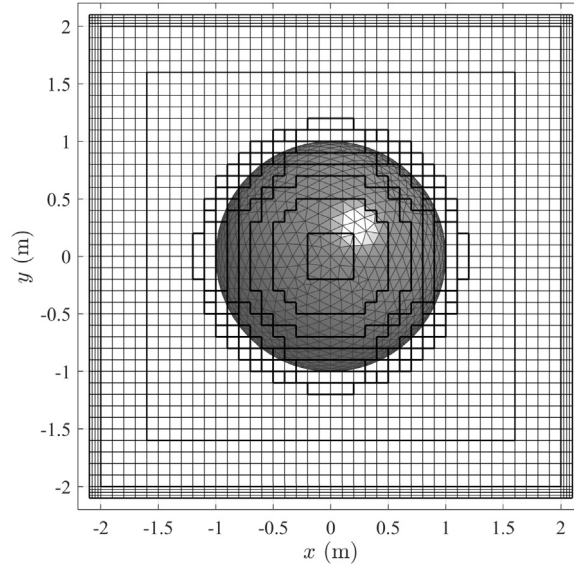
Fig. 3. Computational mesh for the resolution h_4 of the PEC sphere with a triangulated surface Γ_{PEC}. The vicinity of the sphere is discretized by unstructured tetrahedrons, where this mesh is truncated at the staircased hybrid interface indicated by thick solid lines. Outside the hybrid interface, we have the near-to-far-field surface Γ_T and use a discretization of cube-shaped elements. The PML region with PEC backing conforms to the outer box-shaped boundary of the computational domain.
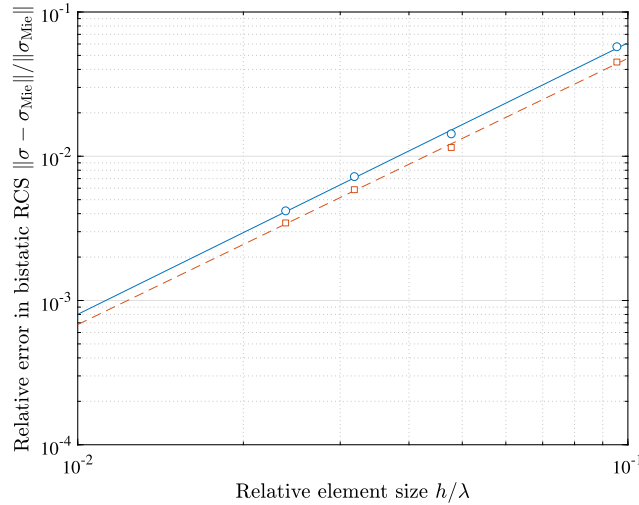
Fig. 4. Relative error in the bistatic radar cross section versus mesh resolution at $k_0 a = 1.5$ for the PEC sphere of radius a: circles – hybrid Huygens' surface; squares – scattered-field formulation. The lines show a least-squares fit of the computed data to the error model $e_{\text{rel}}(h) = ch^\alpha$.

sufficiently small reflection coefficient for the convergence study performed here.) The discretized geometry of the PEC sphere for the mesh with cell size h_4 is shown in Fig. 3, where the staircased hybrid interface is indicated by thick solid lines. Below, the electric field is represented by $p^{\text{hex}} = p^{\text{tet}} = 1_i$ everywhere except for the tetrahedrons' faces that coincide with the hybrid interface Γ_I, where $p^{\text{tet}} = 1_c$ is used.

Fig. 4 shows the relative error $e_{\text{rel}}(h_n) = ||\sigma(h_n) - \sigma_{\text{Mie}}||/||\sigma_{\text{Mie}}||$ for the bistatic radar cross section as a function of the normalized cell size h_n/λ, where we use the norm $||\cdot|| = ((4\pi)^{-1} \int_{\Omega_{4\pi}} (\cdot)^2 \, d\Omega)^{1/2}$ that corresponds to the root mean square (rms) value computed over the solid angle 4π subtended by the full unit sphere $\Omega_{4\pi}$. We show two different methods to illuminate the scatterer by a plane wave: (i) circles – the Huygens' surface presented in this article collocated with the hybrid interface; and (ii) squares – the same hybrid method with $\boldsymbol{P}_H = \boldsymbol{Q}_H = \boldsymbol{0}$ and, instead, a conventional scattered-field formulation imposes the incident field directly on the surface of the sphere by an inhomogeneous Dirichlet boundary condition $\hat{\boldsymbol{n}} \times \boldsymbol{E}^{\text{sca}} = -\hat{\boldsymbol{n}} \times \boldsymbol{E}^{\text{inc}}$. It is clear that the Huygens' surface presented in this article yields an error that is on par with the conventional scattered-field formulation, where the small difference is expected since the scattered-field formulation suffers less from dispersion errors.
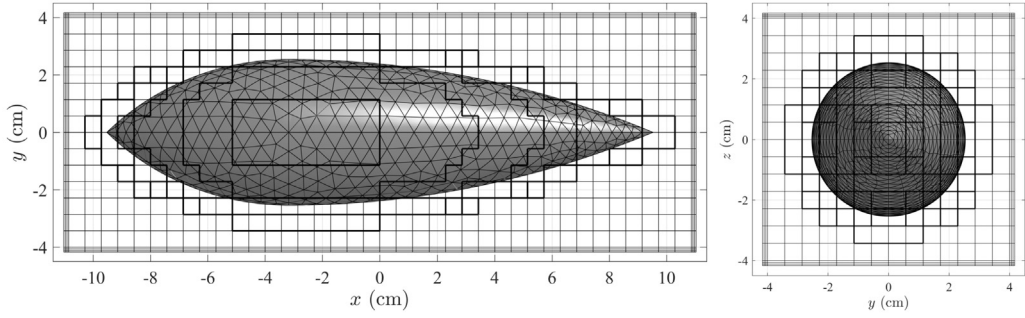
Fig. 5. PEC double ogive and computational domain viewed from the side (left) and from the front (right). The vicinity of the double ogive is discretized by unstructured tetrahedrons, where this mesh is truncated at the staircased hybrid interface indicated by thick solid lines. Outside the hybrid interface, we use a discretization of cube-shaped elements, where the PML region with PEC backing conforms to the outer box-shaped boundary of the computational domain.
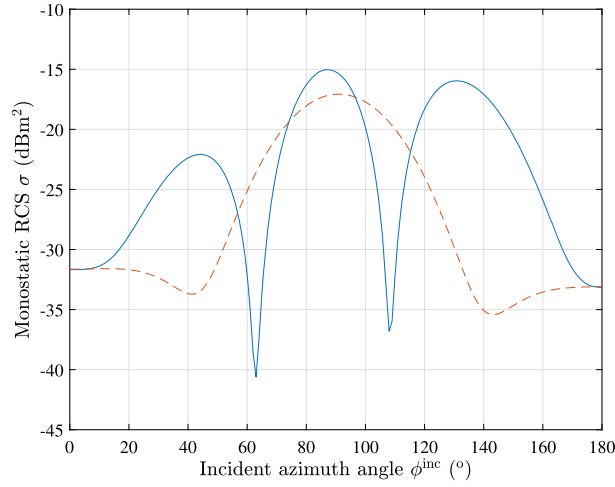
Fig. 6. Monostatic radar cross section versus the azimuth angle ϕ^{inc} for the PEC double ogive at 1.57 GHz: (i) solid curve – the horizontal polarization; dashed curve – the vertical polarization.

In Fig. 4, the lines show a least-squares fit of the error model $e_{\text{rel}}(h) = ch^{\alpha}$ to the computed results and we find that $\alpha \approx 1.9$, which is close to the second-order convergence that is expected for a linear approximation of the electric field applied to a problem without field singularities. The computed radar cross section also compares rather well with earlier works on hybrid formulations for scattering problems [24] that exploit a regular Huygens' surface in the context of the FDTD scheme.

3.2. Double ogive

We also test the proposed Huygens' surface on the PEC double ogive described in Ref. [16], where we compute the monostatic radar cross section at 1.57 GHz and 9 GHz. The monostatic radar cross section of the double ogive is very small for certain angles of incidence, which makes this test case challenging.

Fig. 5 shows a discretization of the double ogive, where the sharp tips support singular field solutions. The total length of the double ogive is 7.5 inch, where the maximum radius is 1 inch perpendicular to the axis of revolution. It consists of two ogival parts that both are generated by revolving a circular arc around the x-axis: (i) the shorter half-ogive has a half length of 2.5 inch and a half angle of 46.4° at its tip; and (ii) the longer half-ogive has a half length of 5 inch and a half angle of 22.6° at its tip. Thus, the double ogive is one wavelength long at the frequency $f = 1.57$ GHz and about 5.7 wavelengths at the frequency $f = 9$ GHz.

Again, we discretize the surface of the PEC scatterer by triangular elements and use an unstructured mesh of tetrahedrons in the vicinity of the double ogive. The hybrid surface is staircased and placed rather close to the double ogive. Here, we collocate both Γ_H and Γ_T with the hybrid interface, which makes the computational mesh relatively small and saves a substantial amount of memory. Outside the hybrid interface (with Γ_H and Γ_T), we use a structured grid of cube-shaped elements. The computational domain is truncated at Γ_{∞} by a PEC with a PML layer.

The computed monostatic radar cross section versus the azimuth angle ϕ^{inc} for the incident plane wave, as it propagates in the horizontal plane $z = 0$, is shown in Fig. 6 for the frequency $f = 1.57$ GHz and Fig. 7 for the frequency $f = 9$ GHz:
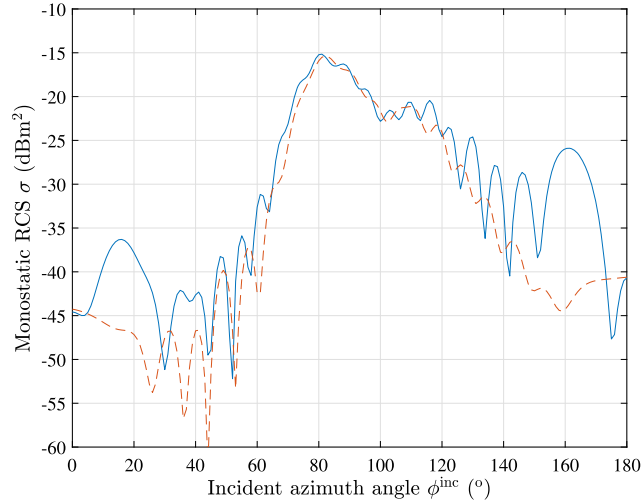
Fig. 7. Monostatic radar cross section versus the azimuth angle ϕ^{inc} for the PEC double ogive at 9 GHz: (i) solid curve – the horizontal polarization; dashed curve – the vertical polarization.

(i) solid curve – horizontal polarization; and (ii) dashed curve – vertical polarization. The two frequencies are analyzed for different settings of the computational parameters: (i) $f = 1.57$ GHz – the electric field and the geometry is represented by linear elements with $\lambda/h \approx 33$ and the PML is described by $L_a = 0.05\lambda$, $N_{PML} = 4$ and $R_0 = 10^{-4}$; and (ii) $f = 9$ GHz – the electric field and the geometry is represented by quadratic elements with $\lambda/h \approx 5.8$ and the PML is described by $L_a = 0.05\lambda$, $N_{PML} = 3$ and $R_0 = 10^{-4}$. For both frequencies, we use an incomplete basis to represent the electric field everywhere, except for tetrahedron faces that coincide with the hybrid interface Γ_I where we enrich the basis with the gradient space to arrive at a complete polynomial approximation of the tangential electric field. The monostatic radar cross section for the double ogive computed by our hybrid method equipped with the proposed Huygens' surface formulation compares very well with both experiments and computations found the open literature [16,25].

4. Conclusion

We present and test a new Huygens' surface formulation for Maxwell's equations, where the equivalent electric and magnetic surface currents on the closed Huygens' surface are incorporated in the finite element method (FEM) by means of Nitsche's method. The method allows for a discontinuous tangential component in the electric field (associated with the equivalent magnetic surface current) on the Huygens' surface, which is accomplished by two sets of degrees of freedom that describe the tangential electric field on the surface. For the rest of the computational domain, we use a curl-conforming representation of the electric field. The weak form is derived based on Nitsche's method, where we employ Galerkin's method and arrive at symmetric discrete operators that preserve the reciprocity of the continuous system. The method features one stabilization parameter and one averaging parameter that can be chosen.

The Huygens' surface formulation is particularly useful in combination with our previously presented higher-order hybridization of a mesh of unstructured tetrahedrons with a Cartesian grid of brick-shaped elements. The brick-shaped elements allow for mass lumping, which reduces memory requirements and is very useful for time-domain computations since it allows for explicit time-stepping. However, the brick-shaped elements are not suited to model complicated geometry and, here, the hybridization with tetrahedrons is very useful since they can conform to complicated surfaces and allow for local mesh-refinement. It is noted that the Huygens' surface formulation presented in this article reduces to this higher-order hybrid formulation as a special case. In addition, the two sets of degrees of freedom for the tangential component of the electric field can be used simultaneously by the Huygens' surface and the hybrid interface, should the two be collocated. Also, we demonstrate that the near-to-far-field transformation surface can be applied to the same closed surface without any significant loss of numerical accuracy, which further reduces the overall memory requirements as the total size of the computational domain can be reduced.

We test the new Huygens' surface formulation with the higher-order brick-tetrahedron hybrid on two scattering problems with perfect electric conductor (PEC) scatterers: (i) a sphere that also allows for an analytical solution and the corresponding assessment of the numerical error; and (ii) a double ogive that features two sharp tips which support field singularities. For all tests, the Huygens' surface is collocated with the hybrid interface between the unstructured mesh of tetrahedrons and the structured grid of brick-shaped elements. In the first test, we study the root-mean-square (rms) error with respect to the scattering angle for the bistatic radar cross section of the PEC sphere, where $k_0 a = 1.5$ given the wavenumber k_0 and the radius a of the PEC sphere. Here, we use the lowest-order elements to represent the electric field throughout the computational domain, where the tetrahedron basis-functions are (locally) complemented to achieve a complete linear

polynomial representation for the tangential electric field at the hybrid interface. A convergence study with respect to the cell size h for the PEC sphere shows that our formulation converges towards the analytical solution with an error that is proportional to h^2. It is also demonstrated that the new Huygens' surface yields a numerical error that is similar to the conventional scattered-field formulation, where the incident field is imposed on the surface of the PEC sphere by means of an inhomogeneous Dirichlet boundary condition. In the second test, the PEC double ogive is analyzed at both 1.57 GHz and 9 GHz, where its electrical length is one wavelength and 5.7 wavelengths respectively. The monostatic radar cross section displays a number of minima with very small values and it is rather low for some relatively large angular intervals, where the angle is measured with respect to the axis of revolution. The low monostatic radar cross section in combination with the field singularities supported by the sharp tips make the PEC double ogive a challenging scattering problem. For both frequencies, the proposed Huygens' surface and the near-to-far-field transformation surface are both collocated with the hybrid brick-tetrahedron interface, which makes it possible to reduce the total number of elements significantly. For the frequency 1.57 GHz, we use the same representation for the electric field as in the first test for the PEC sphere. For the frequency 9 GHz, we use incomplete quadratic elements for both the brick elements and tetrahedrons to express the electric field, where the tetrahedrons are enriched with the gradients that yield a complete quadratic polynomial approximation for the tangential electric field on the brick-tetrahedron interface. We use 33 cells per wavelength at 1.57 GHz. For the frequency 9 GHz, we use a discretization with about 5.8 cells per wavelength, which corresponds to 11.6 points per wavelength for the interpolatory basis of quadratic polynomial order on the brick-shaped elements. At both frequencies, the results compare very well with benchmark radar cross section measurements and computations reported in the open literature.

In conclusion, we find that the new Huygens' surface yields accurate and reliable results, which are in good agreement with important reference solutions found in the open literature. The proposed method may be combined with our higher-order brick-tetrahedron hybrid such that the Huygens' surface can be collocated with both the hybrid interface and the near-to-far-field transformation surface, which is a unique feature for the method presented in this article that cannot be reproduced by other Huygens' surface formulations in the open literature. Thus, the collocation of these three surfaces is new and, for a given scatterer, it allows for a considerably reduction in the total number of elements required, which is very attractive with respect to the efficient usage of both computational time and memory.

CRediT authorship contribution statement

- Johan Winges: derivations, coding, executing tests, producing figures, validation.
- Thomas Rylander: idea, formulation, writing (original manuscript, revised manuscript, etc), supervision, project administration, funding acquisition.

Declaration of competing interest

The authors declare that they have no known competing financial interests or personal relationships that could have appeared to influence the work reported in this paper.

Data availability

The authors are unable or have chosen not to specify which data has been used.

Acknowledgements

References

[1] G. Mie, Beiträge zur Optik trüber Medien, speziell kolloidaler Metallösungen, Ann. Phys. 330 (3) (1908) 377–445.
[2] F.M. Kahnert, Numerical methods in electromagnetic scattering theory, J. Quant. Spectrosc. Radiat. Transf. 79–80 (2003) 775–824.
[3] J.M. Jin, The Finite Element Method in Electromagnetics, 3rd edition, John Wiley & Sons, Hoboken, NJ, 2014.
[4] J.P. Bérenger, A perfectly matched layer for the absorption of electromagnetic waves, J. Comput. Phys. 114 (October 1994) 185–200.
[5] T. Rylander, J.M. Jin, Perfectly matched layer in three dimensions for the time-domain finite element method applied to radiation problems, IEEE Trans. Antennas Propag. 53 (4) (2005) 1489–1499.
[6] G. Cohen, Higher Order Numerical Methods for Transient Wave Equations, Springer, Berlin, 2002.
[7] K.S. Yee, Numerical solution of initial boundary value problems involving Maxwell's equations in isotropic media, IEEE Trans. Antennas Propag. AP-14 (May 1966) 302–307.
[8] A. Taflove, S.C. Hagness, Computational Electrodynamics: The Finite-Difference Time-Domain Method, 3rd edition, Artech House, Boston, MA, 2005.
[9] R.G. Marchand, M.M. Botha, D.B. Davidson, Total and scattered field decomposition for the vector Helmholtz equation using the FETI, Electromagnetics 28 (2008) 77–91.
[10] C. Farhat, F.X. Roux, A method of finite element tearing and interconnecting and its parallel solution algorithm, Int. J. Numer. Methods Eng. 32 (1991) 1205–1227.

[11] J. Nitsche, Über ein Variationsprinzip zur Lösung von Dirichlet-Problemen bei Verwendung von Teilräumen, die keinen Randbedingungen unterworfen sind, Abh. Math. Semin. Univ. Hamb. 36 (1971) 9–15.

[12] P. Hansbo, Nitsche's method for interface problems in computational mechanics, GAMM-Mitt. 28 (2) (2005) 184–207.

[13] J.C. Nédélec, Mixed finite elements in $\mathbb{R}^3$, Numer. Math. 35 (3) (1980) 315–341.

[14] J. Winges, T. Rylander, Higher-order brick-tetrahedron hybrid method for Maxwell's equations in time domain, J. Comput. Phys. 321 (2016) 698–707.

[15] C.A. Balanis, Advanced Engineering Electromagnetics, John Wiley & Sons, New York, NY, 1989.

[16] A.C. Woo, H.T.G. Wang, M.J. Schuh, M.L. Sanders, Benchmark radar targets for the validation of computational electromagnetics programs, IEEE Antennas Propag. Mag. 35 (February 1993) 84–89.

[17] G. Kristensson, Scattering of Electromagnetic Waves by Obstacles, SciTech Publishing, Edison, NJ, 2016.

[18] P. Monk, Finite Element Methods for Maxwell's Equations, Oxford University Press, New York, NY, 2003.

[19] E. Wadbro, S. Zahedi, G. Kreiss, M. Berggren, A uniformly well-conditioned, unfitted Nitsche method for interface problems, BIT Numer. Math. 53 (2013) 791–820.

[20] P. Ingelström, A new set of $\boldsymbol{H}$(curl)-conforming hierarchical basis functions for tetrahedral meshes, IEEE Trans. Microw. Theory Tech. 54 (January 2006) 106–114.

[21] Z.S. Sacks, D.M. Kingsland, R. Lee, J.F. Lee, A perfectly matched anisotropic absorber for use as an absorbing boundary condition, IEEE Trans. Antennas Propag. 43 (December 1995) 1460–1463.

[22] L. Zhao, A.C. Cangellaris, GT-PML: generalized theory of perfectly matched layers and its application to the reflectionless truncation of finite-difference time-domain grids, IEEE Trans. Microw. Theory Tech. 44 (December 1996) 2555–2563.

[23] J.P. Bérenger, Perfectly Matched Layer (PML) for Computational Electromagnetics, Morgan & Claypool Publishers LLC, 2007.

[24] D. Degerfeldt, T. Rylander, Scattering analysis by a stable hybridization of the finite element method and the finite-difference time-domain scheme with a brick-tetrahedron interface, Electromagnetics 28 (1–2) (2008) 3–17.

[25] W. Gibson, The Method of Moments in Electromagnetics, 2nd edition, Taylor & Francis, Boca Raton, FL, 2015.